




# Ti-6Al-4V to over 1.2 TPa: Shock Hugoniot experiments, *ab initio* calculations, and a broad-range multiphase equation of state

Pat Kalita, Kyle R. Cochrane, Marcus D. Knudson, Tommy Ao , Carrie Blada, Jerry Jackson, Jeffrey Gluth , Heath Hanshaw, and Ed Scoglietti   
Sandia National Laboratories, Albuquerque, New Mexico 87125, USA

Scott D. Crockett  
Los Alamos National Laboratory, Los Alamos, New Mexico 87545, USA



(Received 29 September 2022; accepted 30 January 2023; published 1 March 2023)

Titanium alloys are used in a large array of applications. In this work we focus our attention on the most used alloy, Ti-6Al-4V (Ti64), which has excellent mechanical and biocompatibility properties with applications in aerospace, defense, biomedical, and other fields. Here we present high-fidelity experimental shock compression data measured on Sandia's Z machine. We extend the principal shock Hugoniot for Ti64 to more than threefold compression, up to over 1.2 TPa. We use the data to validate our *ab initio* molecular dynamics simulations and to develop a highly reliable, multiphase equation of state (EOS) for Ti64, spanning a broad range of temperature and pressures. The first-principles simulations show very good agreement with Z data and with previous three-stage gas gun data from Sandia's STAR facility. The resulting principal Hugoniot and the broad-range EOS and phase diagram up to 10 TPa and  $10^5$  K are suitable for use in shock experiments and in hydrodynamic simulations. The high-precision experimental results and high-fidelity simulations demonstrate that the Hugoniot of the Ti64 alloy is stiffer than that of pure Ti and reveal that Ti64 melts on the Hugoniot at a significantly lower pressure and temperature than previously modeled.

DOI: [10.1103/PhysRevB.107.094101](https://doi.org/10.1103/PhysRevB.107.094101)

## I. INTRODUCTION

### A. Ti-6Al-4V properties and applications

Unraveling the structure-property-performance relationship of metal alloys subjected to high-pressure and high-temperature conditions is of fundamental importance in the field of condensed matter physics, with numerous technological applications. Appearing in the United States in 1954, Ti-6Al-4V (Ti 90 wt%, Al 6 wt%, V 4 wt%), also called Ti64, remains the most used of titanium alloys in commercial and in industrial applications. It displays excellent mechanical (high strength-to-weight ratio, high fatigue resistance, etc.), biocompatibility properties, and outstanding corrosion resistance together with ease of machinability [1]. Due to its reliable performance Ti-6Al-4V possesses a range of applications in aerospace, automotive, and biomedical (protheses and implants) fields as well as in chemical plant, power generation, oil and gas extraction, sporting goods, and building applications [1].

Pure titanium crystallizes in the  $\alpha$  *hcp* lattice (hexagonal closed packed, structure: space group 194,  $P6_3/mmc$ ) at low and ambient temperature, while at high temperature (1155 K) it transitions to a  $\beta$  *bcc* lattice (body-centered cubic, structure: space group 229,  $Im\bar{3}m$ ). The Ti-6Al-4V alloy is a two-phase alloy of titanium with substitutional aluminum and vanadium. At ambient conditions, Ti64 crystallizes predominantly in the *hcp* lattice, or  $\alpha$  phase, but with a smaller fraction by volume of *bcc* or  $\beta$  phase Ti64 around the  $\alpha$

grain boundaries. In Ti64 the inclusion of aluminum stabilizes the  $\alpha$  phase while the  $\beta$  phase is stabilized by vanadium. Stabilization occurs by increasing or lowering the transition temperature to the  $\beta$  phase through addition of Al or V, respectively. Hence the material is sometimes called an  $\alpha + \beta$  Ti alloy [1,2]. Alloying of the substitutional elements Al and V increases the strength of Ti64 compared to pure titanium [3].

For applications at extreme conditions such as defense, aerospace, or nuclear industries, it is paramount to have a good description of the mechanical response of the Ti64 alloy to extreme pressures and temperatures. Yet the ubiquitous Ti64 alloy is much less studied, compared with the many investigations on pure Ti, including static and shock compression (see, for example, the book chapter by Velisavljevic and references therein [4]).

The Ti64 Hugoniot was only examined in a few shock compression works up to 250 GPa, with most publications focusing on the region up to  $\sim 20$  GPa: Rozenberg *et al.* measured the Hugoniot up to 14 GPa with manganin gauges [5]. Dandekar *et al.* [6] as well as Hopkins and Brar [7] explored the Hugoniot elastic limit up to 13 GPa. Andriot *et al.* measured the Hugoniot up to 64 GPa with velocimetry [8]. Winfree *et al.* extended the Hugoniot EOS of Ti-6Al-4V up to 250 GPa with shock experiments on a three-stage gas gun [9]. Recent works have focused on Ti64 under static compression in a diamond anvil cell [10–12] including high-pressure and temperature measurements [13].

The equation of state (EOS) of a material plays a key role in describing how the material changes volume and temperature during compression. The Hugoniot, in turn, is a key parameter for describing shock compression of a material and therefore a particularly important component of building analytical EOS models. The scarcity of shock compression experimental data above 250 GPa is a limiting factor for developing a truly predictive Ti64 model. In the absence of adequate experimental data to further understand the high-pressure response of this metal alloy, an equation of state (EOS) for Ti64 cannot be constrained and validated.

Here we show, through high-precision shock experiments and high-fidelity simulations, that the shock response of Ti64 is stiffer than in pure Ti and that the melting point on the Hugoniot is at a lower pressure and temperature than previously assumed. We present experimental measurements of the principal Hugoniot of Ti-6Al-4V on shock compression up to 1.27 TPa (or 1,270 GPa) using the Sandia Z machine. We couple experimental data with *ab initio* molecular dynamics (AIMD) simulations, as well as we develop a new broad-range, multiphase SESAME EOS and phase diagram up to 10 TPa and  $10^5$  K. This EOS table is suitable for use in shock experiments and in hydrodynamic simulations requiring a high-accuracy EOS description of Ti64.

### B. Shock compression

Shock compression is the primary method for exploring the extreme thermodynamic states of stress and temperature. A single shock compression experiment consists of the measurement of a material's end state achieved by single shock wave compression at constant velocity, from a given initial (ambient) state. In a simple shock experiment the conservation of mass, momentum, and energy is described by Rankine-Hugoniot jump conditions [14,15] [Eqs. (1)–(3)], where  $P$ ,  $\rho$ , and  $E$  are the pressure, density, and specific internal energy, respectively, of the shocked material relative to its initial state, denoted with the subscript 0.  $P$ ,  $\rho$ , and  $E$  are related by the shock velocity ( $U_S$ ) and particle velocity behind the shock front ( $U_P$ ) of the shock wave:

$$\frac{\rho}{\rho_0} = \frac{U_S}{U_S - U_P}, \quad (1)$$

$$P - P_0 = \rho_0 U_S U_P, \quad (2)$$

$$2(E - E_0) = (P + P_0) \left( \frac{1}{\rho_0} - \frac{1}{\rho} \right). \quad (3)$$

The ‘‘Hugoniot’’ is then defined as a collection of loci of material end states achieved from a given initial state, and in practice it is a collection of  $P$ - $\rho$  data points or  $U_S$ - $U_P$  data points. By definition, the ‘‘principal Hugoniot’’ initiates from ambient conditions, while nonambient initial conditions lead to measuring ‘‘off-Hugoniot’’ states. To describe the Hugoniot from a collection of single shock experiments one must measure two out of the five unknown quantities:  $U_P$ ,  $U_S$ ,  $\rho$ ,  $P$ , or  $E$ . Typically the easiest to measure in a shock experiment is either  $U_P$  or  $U_S$ , but both cannot be measured in one experiment (except in the special case of a symmetric impact, where the sample and the impactor are made of the same material).

Instead, one can use a process in which a well-characterized standard material with a known Hugoniot (Al, Ta, etc.) is used as the impactor material. This allows one to infer the pressure and density of the material of interest: this is called impedance matching with a standard [16]. Current impedance matching techniques utilize Monte Carlo algorithms to propagate uncertainties in Hugoniot states by incorporating all random experimental uncertainties as well as systematic uncertainties from the standard. The process of Monte Carlo impedance matching is detailed in the following section.

## II. EXPERIMENTS ON THE Z MACHINE, VISAR, DATA PROCESSING, AND ANALYSIS

We carried out shock compression experiments using the Sandia National Laboratories’ Z Machine [17]. The Z machine is a pulsed power system capable of producing shaped current pulses and inducing magnetic fields of more than 20 MA and 10 MG, respectively. One can utilize the Z machine to accelerate aluminum flyer plates up to 40 km/s [18] to probe shock Hugoniot states. In this study, the highest velocity achieved was 30.8 km/s. In the present experiments, we generated shocked states from 0.21 TPa up to 1.27 TPa (210 GPa to 1270 GPa) using the two geometries illustrated in Fig. 1: the coaxial geometry and the two-sided stripline geometry for extremely high velocity experiments. The Al flyer plate was shocklessly accelerated toward the target stack composed of a sample of Ti-6Al-4V Grade 5 (Ti-6Al-4V, Grade 5 per ASTM B 348, Al = 6.24 wt%, V = 3.97 wt.%, 300–500  $\mu$ m thickness depending on experiment, 4.43 g/cm<sup>3</sup>) and an alpha-quartz window. While the back side of the flyer was melted by the high driving current, the impact side of the flyer remained at solid density [18], producing a steady shock in the sample upon impact. For example, in the highest pressure shot, the flyer thickness was 1050 ns and the experiment was designed to produce at least 20 ns of steady shock wave, while the actual transit time through the sample was less than 20 ns.

We used two, push-pull velocity interferometer system for any reflector (VISAR, [19,20]) systems with dual velocity per fringe (VPF) capabilities to measure velocity of the flyer plate from rest up to impact with the target (Fig. 1). Three VISAR signals were typically recorded for the sample eliminating ambiguities and providing redundant measurements for improved precision. Typically, three different VPFs were used on each sample and each window above or below the sample, for example, 0.5878 km/s/f, 1.0632 km/s/f, and 1.4317 km/s/f.

Since the sample is opaque to VISAR light, impact time was determined from fiducials observed in transparent windows adjacent to the opaque sample stack. Impact time was then corrected for any measured tilt of the impact plane and for the relative offset of the two windows as compared to the opaque sample (typically a few microns). Shock breakout was directly monitored at the back surface of the opaque sample, through a window. The sample shock velocity ( $U_S$ ) was calculated using the transit time determined from the VISAR fiducials and the measured thickness. The shock wave was also monitored in a thick quartz witness window, which allowed us to determine any necessary correction due to acceleration of the flyer and apply this correction to the  $U_S$

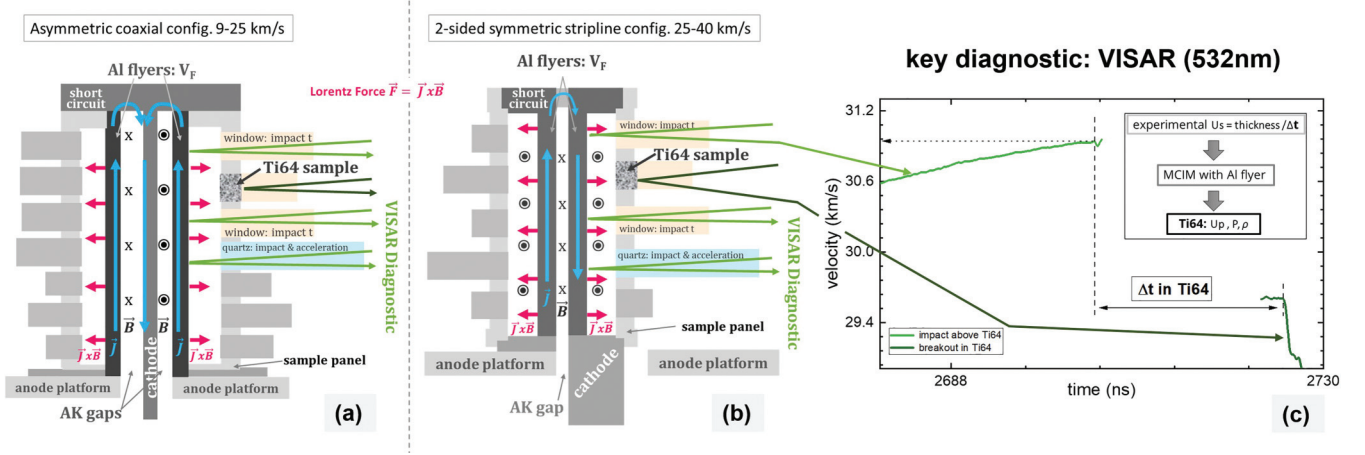


FIG. 1. A shock compression experiment on the Z machine. (a) Schematic of the asymmetric coaxial load configuration for lower velocity experiments and (b) that of the two-sided symmetric stripline configuration for high-velocity experiments, illustrating how flyer acceleration is produced, and the need for multiple VISAR signals. (c) Representative measured VISAR signals from one of the high-velocity experiments on Ti64, and the workflow to obtain a Hugoniot point from the measured quantity  $\Delta t$ .

of the sample. For the transit time measurements, the uncertainty was typically less than 0.5%. In the VISAR analysis, we determined the shock velocity via the transit time using unprocessed VISAR signals. To calculate transit time, we determined when the raw VISAR signal exhibited a change larger than the standard deviation of the signal prior to the change. That marked the impact and the transit into the backing window. The standard deviation from the transit time determination and the uncertainty in the sample thickness was used to determine the uncertainty in the shock velocity. The initial densities of the Ti64 sample and Al flyer plate, the measured flyer velocity at impact ( $V_F$ ), and the inferred  $U_S$  of the sample, enables calculation of the sample Hugoniot state density ( $\rho$ ), pressure ( $P$ ), and particle velocity ( $U_P$ ). The Hugoniot state was determined using a Monte Carlo impedance matching analysis [21,22] to solve the Rankine-Hugoniot equations [Eqs. (1)–(3)] [15]. The Monte Carlo impedance matching (MCIM) method accounts for the correlated and uncorrelated uncertainties in the experimental measurement and the Al Hugoniot standard. In the MCIM, uncorrelated random numbers with one standard deviation equal to the measurement uncertainty were used to perturb the flyer velocity, the shock velocity, and the initial densities about their mean values. Correlated random numbers were used to perturb the fit parameters for the aluminum Hugoniot standard. The linear fit parameters and correlation between the parameters used for the aluminum standard are listed in Table I. The impedance matching calculation was performed to determine  $U_P$ ,  $\rho$ , and  $P$  in the Hugoniot state. The data

TABLE I. Aluminum flyer plate Hugoniot linear fit parameters and covariance matrix parameters for  $U_S = C_0 + S_1 U_P$ .

Flyer	$C_0$ (km/s)	$S_1$	$\sigma_{C_0}^2 \times 10^3$	$\sigma_{S_1}^2 \times 10^3$	$\sigma_{C_0} \sigma_{S_1} \times 10^3$
Al	$6.322 \pm 0.231$	$1.188 \pm 0.020$	53.58	0.4195	-4.605

were saved, and the calculation restarted using new random numbers. A database of Hugoniot states was built for  $10^7$  iterations and the final Hugoniot state was calculated as the mean with one standard deviation of the distribution as the uncertainty. The experimentally determined Hugoniot states with uncertainties are listed in Table II.

### III. *AB INITIO* MOLECULAR DYNAMICS CALCULATIONS

First-principles density functional theory (DFT) was used to conduct *ab initio* molecular dynamics (AIMD) calculations of the Hugoniot using the Vienna *ab initio* simulation package (VASP) [23–26]. The AIMD simulations were performed in the canonical (NVT) ensemble with the Mermin generalization of the Kohn-Sham equations to finite temperature [27]. The exchange-correlation energy was computed with the parameterization of Perdew, Burke, and Ernzerhof (PBE) [28]. In the Kohn-Sham equations, the nuclei were represented by a projector augmented wave (PAW) method [29]. The pseudopotentials contained three electrons, 12 electrons, and 13 electrons for aluminum, titanium, and vanadium, respectively. The cutoff energy was set to 700 eV. The k-point mesh was Monkhorst-Pack [30]  $2 \times 2 \times 2$  for a 128 atom *hcp* reference cell. The vanadium 4 wt% and aluminum 6 wt% were rounded to an integer number of five and 13 atoms, which were substituted randomly into the titanium lattice (Fig. 2), because DFT is not realistically capable of looking at grain boundary effects. The vanadium 4 wt% and aluminum 6 wt% atoms were substituted randomly into the titanium lattice (Fig. 2) using the ATAT code [31]. Three different initial atom position configurations were tested and the difference in energy and pressure between them was negligible. We only examined the  $\alpha$  (*hcp*) phase on the assumption that the vast majority of the material would be in this phase and the contribution to the reference state by the  $\beta$  (*bcc*) BCC grain boundary would be small. The simulation ran for 6 picoseconds at 0.6 fs per time step for ion motion using velocity scaling as the thermostat. The  $6\text{g}/\text{cm}^3$  Hugoniot point is in the  $\omega$  phase,

TABLE II. Experimental data for the principal Hugoniot of Ti-6Al-4V. The initial density was  $4.43 \text{ g/cm}^3$  with an uncertainty of 0.3%.

Flyer	$V_F$ (km/s)	$U_P$ (km/s)	$U_S$ (km/s)	$\rho$ (g/cc)	$P$ (GPa)
Al	$10.50 \pm 0.02$	$4.68 \pm 0.03$	$10.03 \pm 0.04$	$8.31 \pm 0.07$	$208.0 \pm 2.0$
Al	$11.98 \pm 0.04$	$5.30 \pm 0.05$	$10.96 \pm 0.15$	$8.58 \pm 0.18$	$257.4 \pm 2.8$
Al	$12.66 \pm 0.03$	$5.57 \pm 0.04$	$11.45 \pm 0.07$	$8.63 \pm 0.09$	$282.7 \pm 2.1$
Al	$12.88 \pm 0.01$	$5.68 \pm 0.04$	$11.50 \pm 0.09$	$8.76 \pm 0.11$	$289.3 \pm 2.2$
Al	$14.70 \pm 0.01$	$6.46 \pm 0.04$	$12.55 \pm 0.09$	$9.13 \pm 0.11$	$359.0 \pm 3.0$
Al	$17.87 \pm 0.02$	$7.79 \pm 0.05$	$14.44 \pm 0.14$	$9.62 \pm 0.17$	$498.5 \pm 4.1$
Al	$24.04 \pm 0.01$	$10.46 \pm 0.06$	$17.80 \pm 0.12$	$10.75 \pm 0.20$	$825.0 \pm 6.0$
Al	$30.83 \pm 0.06$	$13.43 \pm 0.08$	$21.34 \pm 0.15$	$11.96 \pm 0.22$	$1270.0 \pm 10.0$

so that simulation used 192 atoms. The higher compression simulations were in the liquid phase and used 128 atoms. Hugoniot material states were interpolated from bracketing simulations. Table III lists the calculated Hugoniot states from the present AIMD calculations.

#### IV. DEVELOPMENT OF A BROAD RANGE EOS

We developed a new EOS table in the SESAME format [32,33], SES92966, which gives a broader range of densities and temperatures than was feasible to produce with DFT. A tabular-style EOS like SESAME is often required for many types of simulations. SESAME tables have been used in hydrodynamic calculations since the early 1970s.

In the development of the SESAME EOS (see Fig. 3), we used a standard three-term decomposition of the Helmholtz free energy: cold curve, ion thermal, and electron thermal components, i.e.,  $F(T, V) = F_{\text{cold}}(V) + F_{\text{ion}}(T, V) + F_{\text{electron}}(T, V)$  [33]. The ion thermal component used a Debye approximation for the solid [34] and a corrected Debye [35] approximation for the fluid [36]. The thermodynamic

Grüneisen gamma ( $\gamma_{\text{ref}} = 1.14$ ) and reference Debye temperature ( $\theta_{\text{ref}} = 318 \text{ K}$ ) in the ion thermal model [37] were set by matching isobaric expansion data [38,39] and specific heat [40]. The cold curve, in the form of a Birch-Murnaghan [41] was determined by leveraging diamond anvil cell data and density functional theory results as constraints. The derivative of the Grüneisen gamma ( $\gamma$ ) parameter with respect to density was obtained by matching shock compression data and quantum molecular dynamic calculation in the fluid phase. The electron thermal component was determined using the Thomas-Fermi-Dirac (TFD) model. In the region of the liquid shock data, the free parameters consist of  $g_{\text{ref}}$ ,  $q_{\text{ref}}$ , for the ion model and a fourth-order Birch-Murnaghan cold curve.

#### V. RESULTS AND DISCUSSION: EXPERIMENTAL SHOCK DATA TO OVER 1.2 TPa, AIMD AND EOS

In this section we present the results of the three-pronged approach of this project: experimental shock data to over 1.27 TPa, AIMD modeling to the same pressure and a high-fidelity, multiphase SESAME EOS Ti64.

The experimental Hugoniot data in  $U_S$ - $U_P$  space from the Z machine experiment are presented in Fig. 4. The corresponding experimental  $P$ - $\rho$  states are presented in Fig. 5. We also compare, in Fig. 5, the present Z data and AIMD simulations with: prior gun data from Hopkins [7], Andriot [8], and Winfree [9], as well as with three EOS models: the new SESAME 92966, which is developed in this work, SESAME 2970 for pure Ti [42], and SESAME 4061 for Ti64 [42]. The Z machine Hugoniot data extend from 0.21 TPa to 1.26 TPa and span a range of threefold compression (Figs. 4 and 5). The lowest pressure points from the Z machine (208–257 GPa) overlap with gas gun data from Winfree [9] and hence provide continuity between data from different platforms.

It is straightforward to conclude from the results in Figs. 4 and 5 that the AIMD calculations are in excellent agreement with the experimental data from Z. Because the AIMD is entirely independent from the experimental data, the agreement between theory and experiment provides a high degree of confidence in AIMD calculations. The SESAME 92966 EOS developed in this work is consistent with the Z data and the AIMD calculations, over the range covered by the experiments (Fig. 5). The high precision shock experiments and high-fidelity simulations in Fig 5 all display an increased curvature towards lower densities in  $P$ - $\rho$  space, or stiffening in the Hugoniot with respect to pure Ti (SESAME 2970).

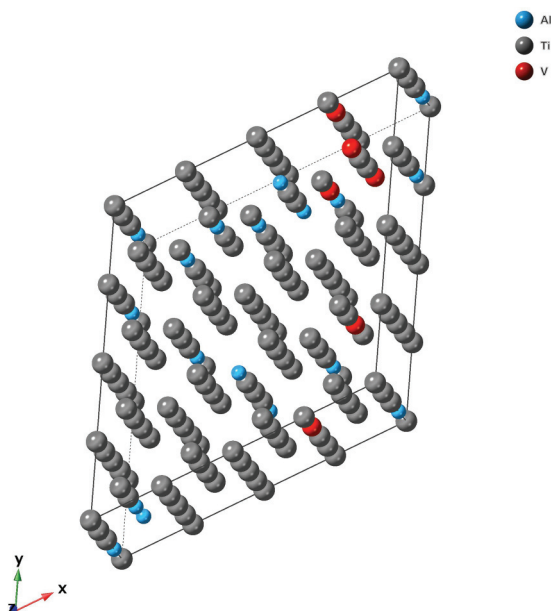


FIG. 2. Representation of the crystal lattice used in the AIMD calculations: Ti: gray speres; Al: blue speres; V: red speres.

TABLE III. DFT-MD Hugoniot data for Ti-6Al-4V.

No. atoms	$\rho$ (g/cm <sup>3</sup> )	$T$ (K)	Pressure (GPa)	Energy (J/kg)	$U_P$ (km/s)	$U_S$ (km/s)
128	5.0	364.4	16.2	$-1.96 \times 10^7$	0.650	5.703
192	6.0	887.5	54.3	$-1.82 \times 10^7$	1.796	6.862
192	7.0	2860.3	110.0	$-1.53 \times 10^7$	3.022	8.232
128	7.5	3951.2	146.6	$-1.31 \times 10^7$	3.683	8.998
128	7.7	4744.4	164.0	$-1.20 \times 10^7$	3.968	9.343
128	8.0	6358.5	194.2	$-1.01 \times 10^7$	4.425	9.917
128	8.3	8409.0	228.1	-7840731	4.902	10.514
128	9.0	14912.4	334.8	-659253.9	6.197	12.204
128	10.0	30714.9	571.5	$1.61 \times 10^7$	8.479	15.222
128	11.0	58752.1	974.6	$4.59 \times 10^7$	11.464	19.195

Examining the Hugoniot in  $U_S-U_P$  space or in  $P-\rho$  space (Figs. 4 and 5) can be a valuable way to identify possible phase transitions, including shock melting. Examples of shock-melt in metals detectable as slight discontinuities in the Hugoniot in  $U_S-U_P$  or a subtle steepening in  $P-\rho$  space are Al [43], Fe [44], Cu [45], and V [46]. In Fig. 4(a) at  $U_P \sim 3.8$  km/s we observe a discontinuity in the Hugoniot, which also appears in Fig. 5 as a subtle steepening in  $P-\rho$  space beginning at  $\rho \sim 7.4$  g/cm<sup>3</sup> or  $P \sim 140$  GPa. This discontinuity likely arises from shock-driven melt in Ti64. It has been proposed [47] that the effects of pressure and material properties on the shock response are more easily seen and analyzed by plotting  $U_S-U_P$  vs  $U_P$ . Such a plot recasts shock velocity in a frame of reference moving with the material behind the shock, i.e., with velocity  $U_P$  and can be very useful to highlight slope changes due to shock-melt transitions [43,47]. Figure 4(b) shows  $U_S-U_P$  as a function of  $U_P$  for Ti64. In Fig. 4(b) we note the very clear change in slope in the region  $U_P \sim 3.8$  km/s (or  $\rho \sim 7.4$  g/cm<sup>3</sup> or  $\sim 130$  GPa), which we interpret as a shock-melt transition.

AIMD simulations were performed near melt for  $\rho = 7.0$  g/cm<sup>3</sup> at 3000 K and 3500 K and 7.5 g/cm<sup>3</sup> at 3700 K and 4000 K. We interpolate along temperature at constant

density for each Hugoniot point. Figure 6 shows the mean atom displacement from two different simulations. The first is at 7.0 g/cm<sup>3</sup> and 3500 K and the second is at 7.5 g/cm<sup>3</sup> and 4000 K. These two simulations were selected as they are at bounding temperatures of our bracketing simulations. Figure 6(a) shows the AIMD simulation at 7.0 g/cm<sup>3</sup> and Fig. 6(b) shows 7.5 g/cm<sup>3</sup>. As can be seen, Ti64 is solid at the lower temperature point, but has begun to melt at 4000K. Also seen in Fig. 6(b) is the species-dependent and independent displacement. The aluminum and vanadium shift as if they are a liquid and then appear remain stationary for some time before moving again. This is due to the low number of atoms (13 Al and 5 V). To test this, we calculated the displacement of the titanium in blocks of 13 atoms and saw similar behavior. When the entire simulation is assumed to be a single species [Fig. 6(b), line marked “combined Al+Ti+V”], this artifact of averaging over few atoms is no longer present. The constant increase in displacement [Fig. 6(b)] is an established signature of a liquid system.

Over the range of all the experimental data from the Z machine and from literature the  $U_S-U_P$  data exhibit a slight curvature (Fig. 4). To facilitate the use of Ti64 as an experimentally constrained impedance matching material, we fit a

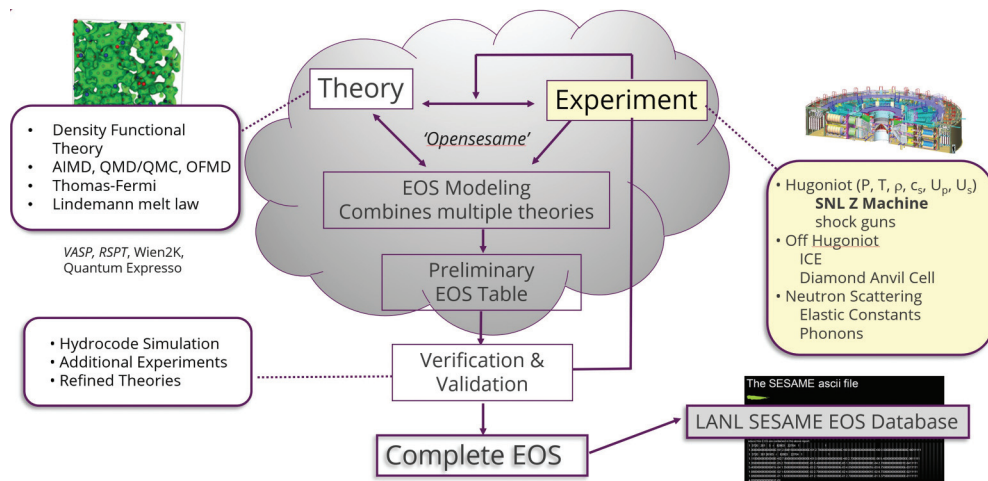


FIG. 3. Workflow involved in the design of a SESAME-style equation of state.

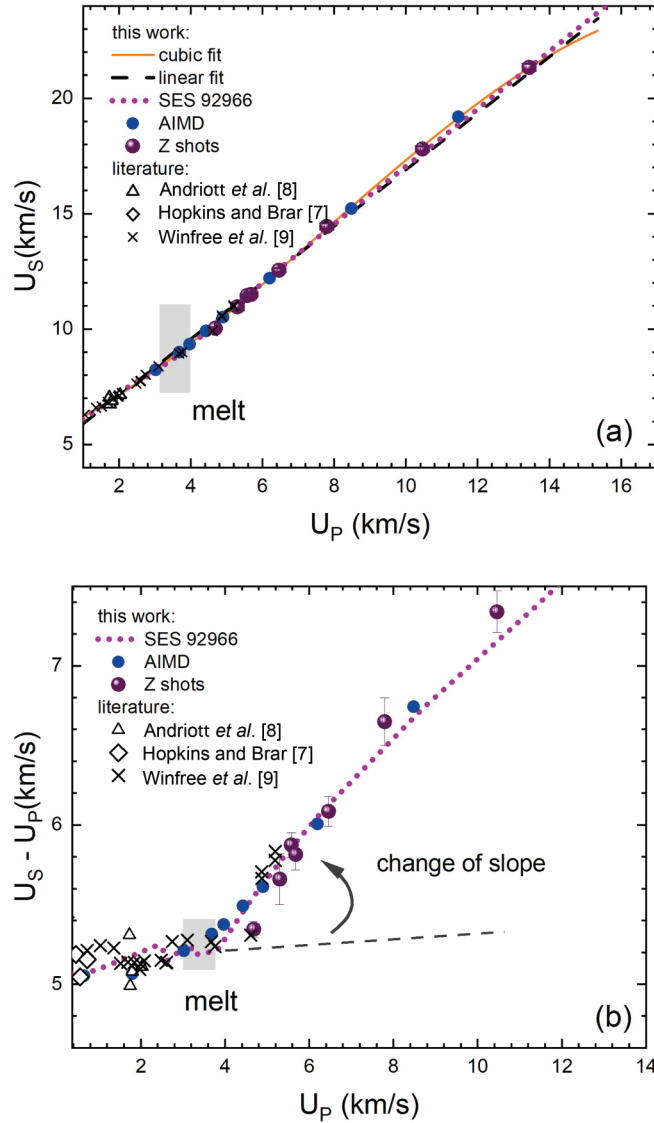


FIG. 4. (a) Ti64 Hugoniot Z data in  $U_S-U_P$  space, alongside AIMD data (this work), SESAME 92966 (this work, dotted purple line), and literature gun data. Also shown are the fits to the data: linear fit (dashed black line) and cubic fit (solid orange line). (b) Plot of  $U_S-U_P$  vs  $U_P$  that highlights the change in slope due to shock melt. The dashed line is a guide to the eye.

cubic polynomial to all experimental data:

$$U_S = C_0 + C_1 U_P + C_2 U_P^2 + C_3 U_P^3. \quad (4)$$

The cubic fit results are listed in Table IV and the covariance matrix elements are listed in Table V. This functional form was chosen because the cubic polynomial captures well

TABLE IV. Parameters for the cubic fit of the Ti64 Hugoniot:  $U_S = C_0 + S_1 U_P + C_2 U_P^2 + C_3 U_P^3$ .

$C_0$ (km/s)	$C_1$ (km/s) <sup>-1</sup>	$C_2$ (km/s) <sup>-2</sup>	$C_3$ (km/s) <sup>-3</sup>
$5.411 \pm 0.082$	$0.709 \pm 0.058$	$0.086 \pm 0.011$	$-0.0037 \pm 5.301 \times 10^{-4}$

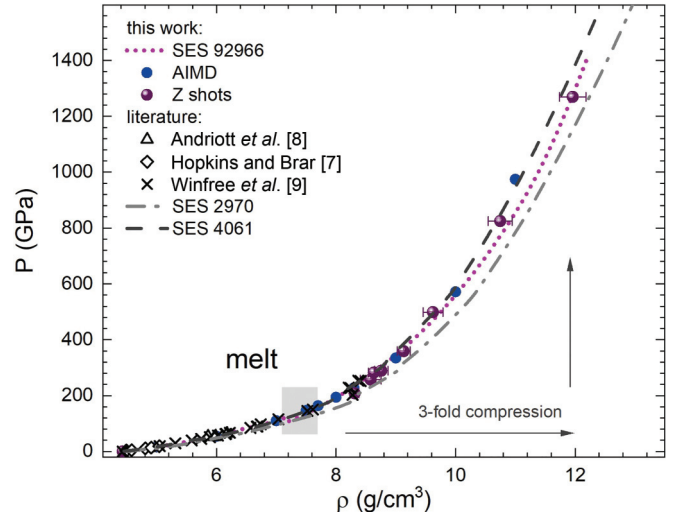


FIG. 5. Ti6Al4V Hugoniot Z data in  $P$ - $\rho$  space, alongside AIMD data and SESAME 92966 (this work), literature gun data, and two SESAME EOS: SEAME 4061 and SESAME 2970 for pure titanium.

the slight curvature in the data and the uncertainty in the fit parameters are well approximated by Gaussian distributions. This polynomial fit is only valid over the range of the experimental data. Since impedance matching with a linear  $U_S-U_P$  is often sufficient for experimental design and simulation of simple configurations, we also list a linear fit to the experimental data from the Z machine and from literature. The linear fit has the advantage of being quick and easy to implement in experiment planning and simulations. Linear fit results and the covariance matrix elements are listed in Table VI.

Finally, putting together the present experimental and AIMD results, in conjunction with the best available experimental data, we generate a new tabular multiphase EOS for

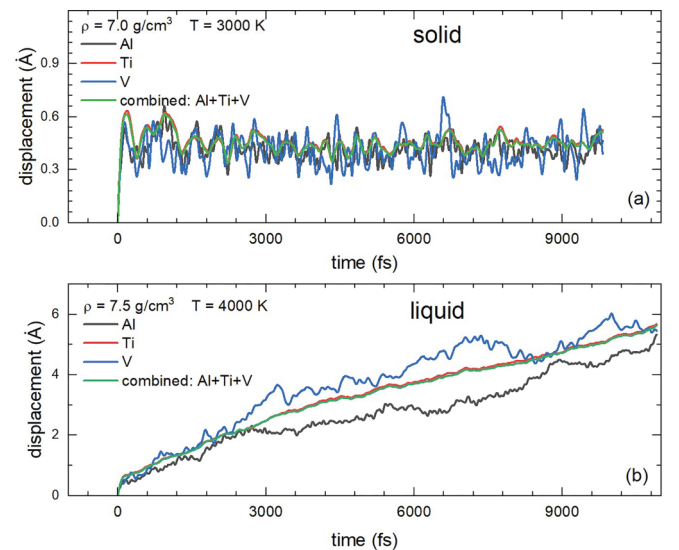


FIG. 6. The mean atom displacement from two different simulations: still solid Ti64 at  $7.0 \text{ g/cm}^3$  at  $3000 \text{ K}$  (top) and Ti64 has begun to melt at  $7.5 \text{ g/cm}^3$  at  $4000 \text{ K}$  (bottom). Single species and combined displacement are shown alongside each other.

TABLE V. Covariance matrix elements for the cubic fit parameters.

	$\sigma_{C0}$	$\sigma_{C1}$	$\sigma_{C2}$	$\sigma_{C3}$
$\sigma_{C0}$	0.0067	-0.00447	$7.69223 \times 10^{-4}$	$-3.58048 \times 10^{-5}$
$\sigma_{C1}$	-0.00447	0.00332	$-6.03258 \times 10^{-4}$	$2.88611 \times 10^{-5}$
$\sigma_{C2}$	$7.69223 \times 10^{-4}$	$-6.03258 \times 10^{-4}$	$1.14434 \times 10^{-4}$	$-5.61709 \times 10^{-6}$
$\sigma_{C3}$	$-3.58048 \times 10^{-5}$	$2.88611 \times 10^{-5}$	$-5.61709 \times 10^{-6}$	$2.80993 \times 10^{-7}$

Ti64. The overall EOS consists of the liquid phase as well as the ambient phase and the higher-pressure crystal phases. The new EOS SESAME 92966 is illustrated in Fig. 7, as a wide-ranging phase diagram of Ti64 spanning 1 TPa and  $10^5$  K. Fig. 7 shows the density and temperature range of the EOS table as well as the assumed phase of the material as a function of pressure and temperature. In the present SESAME 92966 the estimated onset of shock melt on the Hugoniot is  $\sim 110$  GPa and  $\sim 3000$  K (Fig. 7). This is in excellent agreement with the observed discontinuity in the experimental Hugoniot curve (Fig. 4). The AIMD calculations suggest that at 110 GPa the material is still in the solid state; this is consistent with the observation that DFT tends to overestimate melt temperatures [48].

## VI. SUMMARY AND CONCLUSIONS

In this work we examined the shock response of the titanium alloy Ti-6Al-4V (Ti64). New shock Hugoniot data are presented from experiments on the Sandia Z machine. The pressure ranges from 0.21 TPa up to over 1.27 TPa and corresponds to a threefold compression of Ti64. The AIMD calculations are in excellent agreement with the experimental data. We also developed a high-fidelity, multiphase EOS of Ti64, SESAME EOS 92966, spanning a broad range of temperatures and pressures. The resulting Hugoniot is suitable for use in experiments as an impedance matching standard, while the new SESAME EOS is now validated with shock data up to 1.2 TPa and can be used in hydrodynamic simulations involving shock compression of solid materials. The wide-ranging SESAME EOS and phase diagram up to 10 TPa and  $10^5$  K accesses higher density and higher temperature regimes than the AIMD table, thereby allowing simulation of a wider variety of experiments, particularly in regimes where AIMD calculations are computationally intractable.

When comparing the Ti64 Hugoniot obtained in this work with that of pure Ti [42], it is apparent that (Fig. 5) the Ti64 Hugoniot is stiffer with respect to pure Ti, where stiffening corresponds to an increased curvature towards lower densities in  $P$ - $\rho$  space. Previous EOS models predicted [42] a substantial stiffening of the Hugoniot in the alloy, compared to pure Ti. The present Z data and AIMD demonstrate that the stiffening does occur, but to a lesser extent, over the threefold

compression. One can interpret the Hugoniot stiffening in the alloy by considering that, at low compression, the  $P(V)$  Hugoniot and the isentrope are close to each other. Then  $P(V)$  is proportional to  $B(1-V/V_0)$  where  $B$  is the bulk modulus or incompressibility of the material. For a material with a larger bulk modulus, the Hugoniot will then be stiffer, i.e., have a larger  $P(V)$  slope. The bulk modulus for the Ti64 crystal phases ranges from 120 GPa to 156 GPa [13] while pure Ti has smaller bulk moduli ranging from 110 GPa to 130 GPa [49].

Ti64 melt on the Hugoniot was previously suggested [42] to occur at 6000–6800 K and 182–207 GPa, while in pure Ti it was proposed at 6000–7000 K and 178–202 GPa, based on a thermodynamic multiphase model. That model also proposed that shock-melt of Ti64 was likely being underestimated by 10%. Here we present evidence that shock melt of Ti64 is in fact much lower, at  $\rho \sim 7.4$  g/cm<sup>3</sup> or  $\sim 140$  GPa on the Hugoniot. Moreover, a recent experimental work [50] showed that in pure Ti the melt curve follows a much lower  $P$  and  $T$  path. In reference [50] the melt curve for pure Ti was measured experimentally in a diamond anvil cell combined

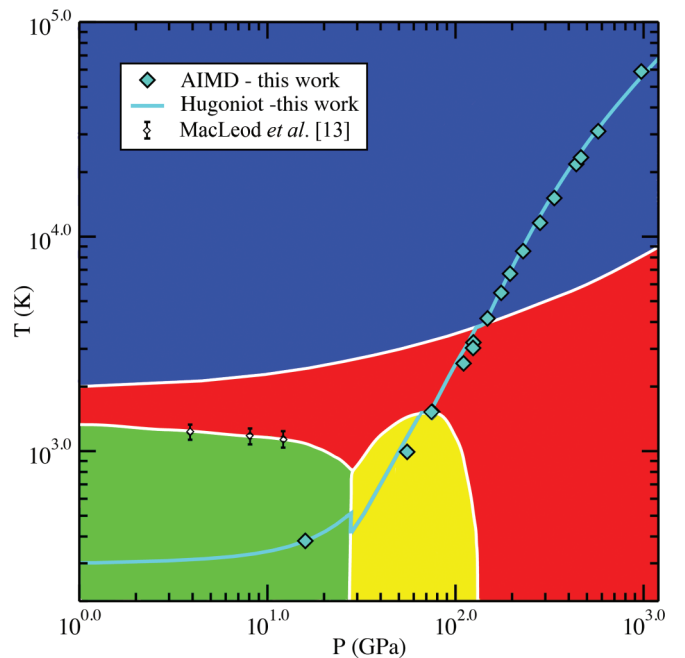


FIG. 7. SESAME EOS 92966 wide-ranging phase diagram of Ti64 spanning 10 TPa and  $10^5$  K. The  $\alpha$  phase is represented in green, the  $\omega$  phase in yellow, the  $\beta$  phase in red, and the liquid in blue. The solid teal curve is the principal Hugoniot with overlapped AIMD calculations (teal diamonds). The  $\alpha$ - $\beta$  phase boundary data points (hollow diamonds) are from Ref. [13].

TABLE VI. Ti64 Hugoniot linear fit parameters and covariance matrix elements for  $U_s = C_0 + S_1 U_p$ .

$C_0$ (km/s)	$S_1$	$\sigma_{C_0}^2 \times 10^5$	$\sigma_{S_1}^2 \times 10^8$	$\sigma_{C_0} \sigma_{S_1} \times 10^7$
$4.672 \pm 0.058$	$1.223 \pm 0.012$	1.156	2.354	3.469

with laser heating and that work reported, at 110 GPa, a range of melt temperatures of 2800–3100 K. The melt curve in Ti64 is expected to be at least similar to that of pure Ti owing to the predominance of Ti in the alloy's composition: for example, at ambient pressure Ti melts at  $\sim 1941$  K and Ti64 at 1943 K [51].

### ACKNOWLEDGMENTS

The authors acknowledge the outstanding work of the Z target fabrication team and the many teams that operate and manage the Z machine. The authors are grateful to Dr. T. R. Mattsson, SNL, for a critical reading of the paper and valuable discussions.

This article has been authored by an employee of National Technology & Engineering Solutions of Sandia, LLC under Contract No. DE-NA0003525 with the U.S. Department of Energy (DOE). The employee owns all right, title and interest in and to the article and is solely responsible for its contents.

The United States Government retains and the publisher, by accepting the article for publication, acknowledges that the United States Government retains a non-exclusive, paid-up, irrevocable, world-wide license to publish or reproduce the published form of this article or allow others to do so, for United States Government purposes. The DOE will provide public access to these results of federally sponsored research in accordance with the DOE Public Access Plan [52].

Sandia National Laboratories is a multimission laboratory managed and operated by National Technology and Engineering Solutions of Sandia, LLC, a wholly owned subsidiary of Honeywell International, Inc., for the U.S. Department of Energy's National Nuclear Security Administration under Contract No. DE-NA-0003525. This paper describes objective technical results and analysis.

Any subjective views or opinions that might be expressed in the paper do not necessarily represent the views of the U.S. Department of Energy or the United States Government.

Work at LANL was supported by the U.S. Department of Energy through Contract No. 89233218NCA000001.

- 
- [1] G. Lütjering and J. C. Williams, *Titanium* (Springer-Verlag, Berlin, 2007).
- [2] C. Veiga, J. P. Davim, and A. J. R. Loureiro, Properties and applications of titanium alloys: A brief review, *Rev. Adv. Mater. Sci.* **32**, 14 (2012).
- [3] M. Peters, J. Hemptenmacher, J. Kumpfert, and C. Leyens, Structure and properties of titanium and titanium alloys, in *Titanium and Titanium Alloys: Fundamentals and Applications*, edited by C. Leyens and M. Peters (Wiley-VCH, Weinheim, 2003), pp. 1–35.
- [4] N. Velisavljevic, S. MacLeod, and H. Cynn, Titanium alloys at extreme pressure conditions, in *Titanium Alloys—Towards Achieving Enhanced Properties for Diversified Applications*, edited by A. K. M. N. Amin (IntechOpen, Rijeka, 2012).
- [5] Z. Rosenberg, Y. Meybar, and D. Yaziv, Measurement of the Hugoniot curve of Ti-6Al-4V with commercial manganin gauges, *J. Phys. D: Appl. Phys.* **14**, 261 (1981).
- [6] D. P. Dandekar and S. V. Spletzer, Shock response of Ti-6Al-4V, *AIP Conf. Proc.* **505**, 427 (2000).
- [7] A. Hopkins and N. S. Brar, Hugoniot and shear strength of titanium 6-4 under shock loading, *AIP Conf. Proc.* **505**, 423 (2000).
- [8] P. Andriot, P. Lalle, and J. P. Dejean, Quasi-elastic behavior of pure titanium and TA6V4 titanium alloy at high pressure, *AIP Conf. Proc.* **309**, 1009 (1994).
- [9] N. A. Winfree, L. C. Chhabildas, W. D. Reinhart, D. E. Carroll, and G. I. Kerley, EOS data of Ti-6Al-4V to impact velocities of 10.4 km/s on a three-stage gun, *AIP Conf. Proc.* **620**, 75 (2002).
- [10] G. N. Chesnut, N. Velisavljevic, and L. Sanchez, Static high pressure x-ray diffraction of Ti-6Al-4V, in *Proceedings of the American Physical Society Topical Group on Shock Compression of Condensed Matter*, edited by M. Elert, M. D. Furnish, R. Chau, N. Holmes, and J. Nguyen (American Institute of Physics, Waikoloa, Hawaii, 2007), pp. 27–30.
- [11] I. Halevy, G. Zamir, M. Winterrose, G. Sanjit, C. R. Grandini, and A. Moreno-Gobbi, Crystallographic structure of Ti-6Al-4V, Ti-HP and Ti-CP under high-pressure, *J. Phys.: Conf. Ser.* **215**, 012013 (2010).
- [12] S. G. MacLeod, B. E. Tegner, H. Cynn, W. J. Evans, J. E. Proctor, M. I. McMahon, and G. J. Ackland, Experimental and theoretical study of Ti-6Al-4V to 220 GPa, *Phys. Rev. B* **85**, 224202 (2012).
- [13] S. G. MacLeod, D. Errandonea, G. A. Cox, H. Cynn, D. Daisenberger, S. E. Finnegan, M. I. McMahon, K. A. Munro, C. Popescu, and C. V. Storm, The phase diagram of Ti-6Al-4V at high-pressures and high-temperatures, *J. Phys.: Condens. Matter* **33**, 154001 (2021).
- [14] G. E. Duvall and R. A. Graham, Phase transitions under shock-wave loading, *Rev. Mod. Phys.* **49**, 523 (1977).
- [15] Y. B. Zel'Dovich and Y. P. Raizer, *Physics of Shock Waves and High Temperature Phenomena* (Dover Publications, Mineola, NY, 2002).
- [16] M. B. Boslough and J. R. Asay, Basic principles of shock compression, in *High-Pressure Shock Compression of Solids*, edited by J. R. Asay and M. Shahinpoor (Springer, New York, 1993), pp. 7–42.
- [17] D. B. Sinars, M. A. Sweeney, C. S. Alexander, D. J. Ampleford, T. Ao, J. P. Apruzese, C. Aragon, D. J. Armstrong, K. N. Austin, T. J. Awe *et al.*, Review of pulsed power-driven high energy density physics research on Z at Sandia, *Phys. Plasmas* **27**, 070501 (2020).
- [18] R. W. Lemke, M. D. Knudson, D. E. Bliss, K. Cochrane, J.-P. Davis, A. A. Giunta, H. C. Harjes, and S. A. Slutz, Magnetically accelerated, ultrahigh velocity flyer plates for shock wave experiments, *J. Appl. Phys.* **98**, 073530 (2005).
- [19] L. M. Barker and R. E. Hollenbach, Laser interferometer for measuring high velocities of any reflecting surface, *J. Appl. Phys.* **43**, 4669 (1972).
- [20] L. M. Barker and K. W. Schuler, Correction to the velocity-perfringe relationship for the VISAR interferometer, *J. Appl. Phys.* **45**, 3692 (1974).
- [21] S. Root, K. R. Cochrane, J. H. Carpenter, and T. R. Mattsson, Carbon dioxide shock and reshock equation of state data to 8



- Mbar: Experiments and simulations, *Phys. Rev. B* **87**, 224102 (2013).
- [22] S. Root, L. Shulenburger, R. W. Lemke, D. H. Dolan, T. R. Mattsson, and M. P. Desjarlais, Shock Response and Phase Transitions of MgO at Planetary Impact Conditions, *Phys. Rev. Lett.* **115**, 198501 (2015).
- [23] G. Kresse and J. Hafner, *Ab initio* molecular dynamics for liquid metals, *Phys. Rev. B* **47**, 558 (1993).
- [24] G. Kresse and J. Hafner, *Ab initio* molecular-dynamics simulation of the liquid-metal–amorphous-semiconductor transition in germanium, *Phys. Rev. B* **49**, 14251 (1994).
- [25] G. Kresse and J. Furthmüller, Efficient iterative schemes for *ab initio* total-energy calculations using a plane-wave basis set, *Phys. Rev. B* **54**, 11169 (1996).
- [26] G. Kresse and J. Furthmüller, Efficiency of *ab-initio* total energy calculations for metals and semiconductors using a plane-wave basis set, *Comput. Mater. Sci.* **6**, 15 (1996).
- [27] N. D. Mermin, Thermal properties of the inhomogeneous electron gas, *Phys. Rev.* **137**, A1441 (1965).
- [28] J. P. Perdew, A. Ruzsinszky, G. I. Csonka, O. A. Vydrov, G. E. Scuseria, L. A. Constantin, X. Zhou, and K. Burke, Restoring the Density-Gradient Expansion for Exchange in Solids and Surfaces, *Phys. Rev. Lett.* **100**, 136406 (2008).
- [29] P. E. Blöchl, Projector augmented-wave method, *Phys. Rev. B* **50**, 17953 (1994).
- [30] H. J. Monkhorst and J. D. Pack, Special points for Brillouin-zone integrations, *Phys. Rev. B* **13**, 5188 (1976).
- [31] A. van de Walle, P. Tiwary, M. de Jong, D. L. Olmsted, M. Asta, A. Dick, D. Shin, Y. Wang, L. Q. Chen, and Z. K. Liu, Efficient stochastic generation of special quasirandom structures, *Calphad* **42**, 13 (2013).
- [32] Specific SESAME EOS requests can be made via the LANL website: <https://www.lanl.gov/org/ddste/aldsc/theoretical/physics-chemistry-materials/sesame-database.php>.
- [33] S. P. Lyon and J. D. Johnson, *T-1 Handbook, the SESAME Equation of State Library* (Los Alamos National Laboratory, Los Alamos, NM, 1998).
- [34] C. Kittel, *Introduction to Solid State Physics* (John Wiley, New York, 2005).
- [35] P. Debye, Zur Theorie der spezifischen Wärmen, *Ann. Phys.* **344**, 789 (1912).
- [36] J. D. Johnson, A generic model for the ionic contribution to the equation of state, *High Pressure Res.* **6**, 277 (1991).
- [37] S. L. Thompson and H. S. Lauson, Improvements in the CHART D radiation-hydrodynamic code III: Revised analytic equations of state, Technical Report # SC-RR-71-0714, United States (1974).
- [38] A. Schmon, K. Aziz, and G. Pottlacher, Density of liquid Ti-6Al-4V, *EPJ Web Conf.* **151**, 04003 (2017).
- [39] J. J. Z. Li, W. L. Johnson, and W.-K. Rhim, Thermal expansion of liquid Ti–6Al–4V measured by electrostatic levitation, *Appl. Phys. Lett.* **89**, 111913 (2006).
- [40] CINDAS LLC, Global benchmark for critically evaluated materials properties data, [https://cindasdata.com/Applications/TPMD/?subaction=&mgcode=TG75&mcode=ta001&prop\\_and\\_indvar=0102c%3A0601](https://cindasdata.com/Applications/TPMD/?subaction=&mgcode=TG75&mcode=ta001&prop_and_indvar=0102c%3A0601).
- [41] F. D. Murnaghan, The compressibility of media under extreme pressures, *Proc. Natl. Acad. Sci. USA* **30**, 244 (1944).
- [42] G. I. Kerley, Equations of state for titanium and Ti6Al4V alloy, SAND Report no. SAND2003-3785 (Sandia National Laboratories, Albuquerque, NM, 2003).
- [43] T. Sjostrom, S. Crockett, and S. Rudin, Multiphase aluminum equations of state via density functional theory, *Phys. Rev. B* **94**, 144101 (2016).
- [44] R. S. Hixson and J. N. Fritz, Shock Compression of Iron, in *Shock Compression of Condensed Matter—1991*, edited by S. C. Schmidt, R. D. Dick, J. W. Forbes, and D. G. Tasker (Elsevier, Amsterdam, 1992), pp. 69–70.
- [45] S. D. Crockett, C. W. Greeff, J. D. Johnson, and L. Burakovsky, Testing of a liquid equation of state model against copper data, *AIP Conf. Proc.* **845**, 65 (2006).
- [46] P. F. Weck, P. E. Kalita, T. Ao, S. D. Crockett, S. Root, and K. R. Cochrane, Shock compression of vanadium at extremes: Theory and experiment, *Phys. Rev. B* **102**, 184109 (2020).
- [47] G. I. Kerley, The linear US-uP relation in shock-wave physics, *arXiv:1306.6916* (2006).
- [48] J. Bouchet, F. Bottin, G. Jomard, and G. Zérah, Melting curve of aluminum up to 300 GPa obtained through *ab initio* molecular dynamics simulations, *Phys. Rev. B* **80**, 094102 (2009).
- [49] A. Dewaele, V. Stutzmann, J. Bouchet, F. Bottin, F. Occelli, and M. Mezouar, High pressure-temperature phase diagram and equation of state of titanium, *Phys. Rev. B* **91**, 134108 (2015).
- [50] V. Stutzmann, A. Dewaele, J. Bouchet, F. Bottin, and M. Mezouar, High-pressure melting curve of titanium, *Phys. Rev. B* **92**, 224110 (2015).
- [51] A. Cezairliyan, J. L. McClure, and R. Taylor, Thermophysical measurements on 90Ti-6Al-4V alloy above 1450 K using a transient (subsecond) technique, *J. Res. Natl. Bur. Stand A* **81A**, 251 (1977).
- [52] <https://www.energy.gov/downloads/doe-public-access-plan>.